Review article

# A systematic review of lumped-parameter equivalent circuit models for real-time estimation of lithium-ion battery states

S. Nejad, D.T. Gladwin[*], D.A. Stone

Department of Electronic and Electrical Engineering, University of Sheffield, Sheffield, S1 3JD, United Kingdom

## HIGHLIGHTS

- Ten lumped-parameter lithium-ion battery models are systematically reviewed.
- Two variations of lithium-ion cells are used for experimental verifications.
- Real-time system identification is realised using dual Extended Kalman filtering.
- Modelling accuracies are compared for online state-of-charge and power predictions.
- Resistor-capacitor network models are shown to have better dynamic performances.

## ARTICLE INFO

## ABSTRACT

This paper presents a systematic review for the most commonly used lumped-parameter equivalent circuit model structures in lithium-ion battery energy storage applications. These models include the Combined model, Rint model, two hysteresis models, Randles' model, a modified Randles' model and two resistor-capacitor (RC) network models with and without hysteresis included. Two variations of the lithium-ion cell chemistry, namely the lithium-ion iron phosphate (LiFePO$_4$) and lithium nickel-manganese-cobalt oxide (LiNMC) are used for testing purposes. The model parameters and states are recursively estimated using a nonlinear system identification technique based on the dual Extended Kalman Filter (dual-EKF) algorithm. The dynamic performance of the model structures are verified using the results obtained from a self-designed pulsed-current test and an electric vehicle (EV) drive cycle based on the New European Drive Cycle (NEDC) profile over a range of operating temperatures. Analysis on the ten model structures are conducted with respect to state-of-charge (SOC) and state-of-power (SOP) estimation with erroneous initial conditions. Comparatively, both RC model structures provide the best dynamic performance, with an outstanding SOC estimation accuracy. For those cell chemistries with large inherent hysteresis levels (e.g. LiFePO$_4$), the RC model with only one time constant is combined with a dynamic hysteresis model to further enhance the performance of the SOC estimator.

© 2016 Elsevier B.V. All rights reserved.

## 1. Introduction

Due to the growing concerns over the emissions of greenhouse gasses, together with the volatile and ever-increasing cost of fossil fuels, a global shift towards hybrid electric vehicles (HEVs), plug-in hybrid electric vehicles (PHEVs) and battery electric vehicles (BEVs) is apparent. The uptake of these electrified vehicles (EVs) within the transport system not only improves the air quality in dense urban areas, but can also provide a distributed energy storage solution for the implementation of the rapidly evolving smart grid [1]. However, without significant improvements on traction battery technologies and battery management systems (BMSs), the adoption of EVs by consumers is not feasible.

A key function of the BMS is to assess and monitor the performance of the traction battery through accurate characterisation of various battery states. These states include the state-of-charge (SOC—quantity of deliverable ampere-hour charge at any time), state-of-health (SOH—ability of a battery to provide its nominal capacity over its service lifetime), state-of-power (SOP—a quantity describing the battery's power capability) and the state-of-function (SOF—a binary yes/no parameter indicating the battery's ability to complete a task) [2—4].

* Corresponding author.
  E-mail addresses: s.nejad@sheffield.ac.uk (S. Nejad), d.gladwin@sheffield.ac.uk (D.T. Gladwin), d.a.stone@sheffield.ac.uk (D.A. Stone).

Whilst direct measurement techniques such as coulomb-counting (integration of battery current over the charge or discharge period) are easy to implement for SOC estimation, they suffer largely from erroneous initialisation of SOC, drifts caused by current sensor noise and battery capacity variations due to temperature and SOH. Moreover, the direct measurement of the other battery states of interest (i.e. SOH, SOP and SOF) for real-time applications is somewhat impossible. Hence, battery models are often utilised within the BMS to indirectly infer and monitor the battery's operation through the measurement of its terminal voltage, current and surface temperature. In addition to accurate characterisation of the battery states, a candidate model is also desired to be computationally efficient. In other words, there should be a balance between model accuracy and complexity so that it can easily be embedded on a simple and inexpensive microprocessor unit (MCU), similar to those found in EV BMS hardware.

The battery models presented in literature mainly fall into one of the following categories:

1. Electrochemical or physics-based models,
2. Empirical or data-based models, and
3. Equivalent electrical-circuit based models.

Electrochemical models (e.g. Refs. [5–9]) that aim to capture the dynamic behaviour of battery cells on a macroscopic scale often can achieve high accuracies. These models are defined by a high number of partial differential equations (PDEs) that must be solved simultaneously. The complexity of any electrochemical model is directly related to the number and order of the governing PDEs, which can lead to tremendous requirements for memory and computational power. Another issue that often precludes these models from real-time applications is that due to the large number of unknown variables, they are likely to run into over-fitting problems, increasing the uncertainty in the model's output. Alternatively, these models can be represented by a lower number of 'reduced order' PDEs and by substituting boundary conditions and discretisation, real-time applications may become achievable (e.g. Refs. [10–12]). However, this comes at the expense of reduced SOC accuracy and yet the computational burden on the MCU remains questionable.

Data-based models (e.g. Refs. [13–15]) often adopt empirically derived equations from experimental data fittings to infer relationships between various battery parameters such as the terminal voltage, throughput current, surface temperature and SOC. Although these models benefit from simplicity and ease of implementation, they often suffer from inaccuracies of 5–20% mainly due to the highly non-linear behaviour of a battery under a dynamic load profile. In Refs. [16,17], the authors took a multiple-model approach to battery modelling using the local model networks (LMN). This technique interpolates between different local linear models to capture the battery's non-linearity due to SOC variations, relaxation, hysteresis, temperature and the battery current effects. One downside of the LMN modelling approach is the excessive requirements for different experiments to train the model in first place. Generally, the data-based model parameters are not physically interpretable, which drops their popularity for *in situ* estimation and tracking of SOH and SOP. Furthermore, a large cell sample of the same chemistry is required to create a dataset for identification and training of data-based models.

In Refs. [18–20], Plett used a series of models including the combined, simple, zero-state hysteresis, one-state hysteresis and a non-linear enhanced self-correcting (ESC) model to adaptively estimate the battery's SOC. The latter model took into consideration the effects of the current direction, the SOC dependency of open-circuit-voltage (OCV) hysteresis and the relaxation or the charge-recovery effect to improve the model accuracy for dynamic load profiles. In an attempt to model the OCV hysteresis behaviour together with the charge recovery effects, Roscher et al. [21] developed an empirical model whose parameters required off-line identification. In Refs. [22], Huria et al. proposed a mathematical model to describe the dynamics of the large hysteresis levels that exist amongst high-power lithium-ion cells. Further on in the paper, this model structure will be referred to as the adaptive hysteresis model.

The lumped-parameter equivalent circuit models have gained a lot of interest amongst EV designers for real-time battery state estimation and power management purposes. This is due to their simplified mathematical and numerical approaches that minimise the necessity for computationally intensive procedures. Furthermore, there is often a strong physical relation between the constituent model parameters and the underlying electrochemical processes that occur within the battery cells. These models use passive electrical components, such as resistors and capacitors, to mimic the behavioural response of a battery. The simplest equivalent circuit model is in the form of an ideal voltage source in series with a resistor [23]. This model assumes that the demand current has no physical influence on the battery, i.e. no core temperature variations or undesired transition effects. More complicated equivalent circuit models include resistor-capacitor (RC) networks to characterise the battery transient responses with different time-constants associated with the diffusion and charge-transfer processes. Depending on the dynamics of the load profile and the required modelling accuracy, the number of the parallel RC branches may vary from one-RC (e.g. Refs. [24–27]) to two-RC (e.g. Refs. [28–30]). Higher order Models of up to fifth-order have also been used previously in literature (e.g. Ref. [31]) to improve the model's impedance response under higher frequencies of operation.

In literature, there are no studies that compare the accuracy and universality of the reported battery models for real-time estimation of SOC and SOP together. Therefore, this review paper aims to carry out a systematic study of a number of selected lumped-parameter battery models for two variations of the lithium-ion cell chemistry, namely the lithium-ion iron phosphate (LiFePO$_4$) and the lithium nickel-manganese-cobalt oxide (LiNMC). The models of interest in this paper include the combined model, Rint model, One-state hysteresis model by Plett, Huria et al. hysteresis model, one- and two-RC models and one- and two-RC models combined with the hysteresis model proposed by Huria et al. [22]. These models were nominated based on the number of their appearances in the literature. The Kalman filter (KF) algorithm is then applied to simultaneously estimate and identify the model parameters in real time. Nevertheless, for those models that are non-linear in parameters (e.g. one- and two-RC models) the extended Kalman filter (EKF) algorithm is adopted.

This paper is organised as follows. Section 2 describes the experimental configuration for gathering an accurate dataset for both training and verification purposes. Section 3 gives a quantitative definition for the SOC, SOP and SOF. Section 4 provides an overview of the battery model structures of interest in this work. Section 5 describes the real-time system identification technique based on the dual-EKF algorithm for both model parameter identification and battery state estimation. Section 6 compares the voltage prediction and SOC estimation capabilities of the nominated model structures. Furthermore, an optimum model structure will be put forward for real-time SOP and SOF estimation. And finally section 7 concludes this paper.

## 2. Battery dataset generation

### 2.1. Experimental setup

The experimental setup features a multi-channel Maccor battery

tester, a built-in-house thermal chamber and a host computer for rig control and data storage. The voltage and current sensors incorporated into each channel of the Maccor system have accuracies of ±0.02% (0–20 V full-scale) and ±0.05% (0–10 A full-scale) respectively. Since the current sensor noise is very small and the sampling rate is reasonably high ($T_s = 100$ ms), it is safe to assume that the integral of the throughput current over the discharge/charge period represents a "true" measurement of the cell's SOC. Therefore, we use the coulomb-counting technique to systematically compare the accuracy of the model-based SOC estimates.

The generality of the candidate battery models are demonstrated using two variations of the lithium-ion cell chemistry, (i.e. LiFePO$_4$ and LiNMC). The specifications for the test cells are presented in Table 1. Three cells of each type are used in this work. One reference cell is used for training purposes and the other two cells are used for model verification.

In order to gather an accurate dataset, a test sequence as presented in Table 2, is designed and implemented. The test sequence starts with incubating the cells in the thermal chamber for 24 h. The chosen dwell time is long enough for the small cylindrical cells to reach a thermal equilibrium prior to any characterisation test. Five temperature settings of 5 °C, 15 °C, 25 °C, 35 °C and 45 °C are chosen for comparison of the model performances across various operating conditions. Throughout the tests, the thermal distribution over the cells is assumed constant and the internal temperature variations due to high discharge/charge currents are neglected.

## 2.2. Capacity test

Initially, each cell undergoes a capacity measurement cycle, which consists of a 0.5C constant-current discharge until the end-of-discharge voltage has been reached. This is to remove any residual charge left in the cell. After a 60 min rest period, the cell is re-charged using the standard constant-current constant-voltage (CCCV) scheme at the manufacturer's recommend current and voltage levels. Following a 60 min rest, the cell under test is discharged at a 0.5C current level. The quantity of charge removed from the cell is recorded as the maximum discharge capacity at the set temperature, which will be used for SOC calculations.

## 2.3. OCV-SOC relationship

In order to generate a function to describe the OCV-SOC relationship, the reference cells were applied with a pulsed-current and relaxation test. The test profile began with a full discharge at a constant current of 0.5C until the lower voltage thresholds were reached. Then, the cells were re-charged to 100% SOC using the CCCV charging scheme. After a relaxation period of 60 min, the first OCV was recorded at SOC = 100%. Furthermore, the cells were discharged in steps of 10% SOC at a current level of 0.5C for both cell chemistries followed by 60 min rest periods. This sequence was repeated until the cells were fully discharged. The OCV measurements during the charge half-cycle were also obtained using a similar procedure, where the cells were charged in steps of 10% SOC at a constant current of 0.5C.

**Table 1**
Specifications for the test cells at 25 °C.

| Parameter | LiFePO$_4$ | LiNMC |
|---|---|---|
| Rated capacity | 3300 mAh | 3600 mAh |
| Nominal voltage | 3.2 V | 3.65 V |
| End-of-Charge voltage | 3.65 V | 4.2 V |
| End-of-discharge voltage | 2.0 V | 2.75 V |
| Nominal resistance | 30 mΩ | 20 mΩ |

**Table 2**
Battery testing procedures.

| Step | Procedure |
|---|---|
| 1. | Set temperature |
| 2. | Capacity test |
| 3. | OCV vs. SOC test |
| 4. | HPPC test |
| 5. | Self-designed pulse test |
| 6. | Multi-cycle NEDC test |

Upon the completion of the pulsed-current test, the OCV values extracted for both the charge and discharge regimes were used to curve-fit an 8th order polynomial function to describe the average OCV-SOC relationship for both the LiFePO$_4$ and LiNMC cells as,

$$V_{OC} = a_8 SOC^8 + \cdots + a_1 SOC + a_0 \qquad (1)$$

The fitted OCV curves at various temperatures are presented in Fig. 1. As can be seen, during the operational SOC range of both battery chemistries (i.e. 20% ≤ SOC ≤ 80%), the OCV-SOC relationship is almost independent of the operating temperature. This finding implies that for practical purposes, one can safely rely on only an OCV curve obtained at a reasonable temperature. However, to keep the modelling uncertainties at a minimum, separate functions are fitted in this work to represent the OCV-SOC relationship at each temperature setting.

## 2.4. HPPC test

The Hybrid-Pulse-Power-Characterisation (HPPC) test is a standard procedure developed by the Partnership for New Generation Vehicles (PNGV) [32] used to determine the power and energy capability of a rechargeable battery under both discharge and regenerative charging scenarios. This particular test profile is used in this work to demonstrate the SOP variability as a function of SOC and operating temperature. It should be noted that the profile starts
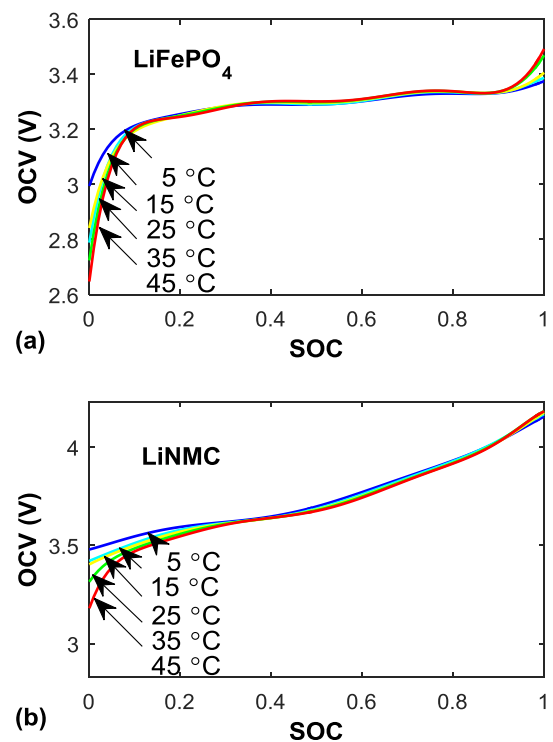


**Fig. 1.** The average OCV-SOC relationship for (a) LiFePO$_4$ and (b) LiNMC reference cells.

with a preamble discharge and re-charge step as to adjust the cell's SOC to 100% prior to testing. Furthermore the HPPC pulses, as shown in Fig. 2(a), are applied over the SOC range of 10–90% in steps of 10% SOC. A discharge current pulse of 0.5C is used for both cell chemistries to take the SOC to the next desired level and a 60 min rest interval is allowed between the HPPC pulse repetitions.

## 2.5. Validation datasets

The validation datasets in this work include the results from a self-designed pulsed-current test and a multi-cycle New European Drive Cycle (NEDC) test. The purpose of the self-designed pulsed-current test, as shown in Fig. 2(b), is to dynamically excite the cell under test with variable current amplitudes and durations. Note that the self-designed test profile has a predominant discharge characteristic as to remove charge from the cell under test. The obtained dataset from this test will be used to compare the output accuracy of the model structures under review.

The multi-cycle NEDC test profile is used to evaluate the adaptability of the battery models for real-time SOC estimation. The test profile starts by removing charge form the cell using a 0.5C current level for both cell chemistries. This step ensures a known



**(a)**

**(b)**

**(c)**

**Fig. 2.** Current profiles for a single repetition of the (a) HPPC, (b) self-designed pulsed-current and (c) multi-cycle NEDC test procedures.

initial SOC value of 90% is achieved prior to applying the cell under test with 14 consecutive NEDC cycles. A single repetition of the NEDC cycle is illustrated in Fig. 2(c). Upon the completion of every NEDC cycle, a rest period of 15 min is allowed before the next cycle commences. Finally, a discharge current pulse of 0.5C is applied as to fully discharge the cell.

## 3. State definitions

In this paper, SOC is defined as.

$$SOC(t) = SOC(0) - \frac{\eta_i}{Q_n} \int_0^t i(\tau) \cdot d\tau \qquad (2)$$

where $\eta_i$ is the cell's Coulombic efficiency of the cell, $i(t)$ is the instantaneous current and $Q_n = 3600 \times Ah$ is the cell's nominal ampere-hour (Ah) capacity. Conventionally, $\eta_i$ is defined as the ratio of the quantity of charge that is injected into a cell during charging to that removed from the cell during discharging.

$$\eta_i = \frac{Q_{discharge}(Ah)}{Q_{charge}(Ah)} \times 100\%. \qquad (3)$$

In order to include SOC as an estimable state in the battery models' state-space equations, the coulomb-counter equation given in (2) needs to be converted into discrete form. Thus, assuming a small sampling period (i.e. $T_s = \Delta t \leq 1$ s) and using a rectangular approximation for $SOC(t)$ yields,

$$SOC_{k+1} = SOC_k - \left(\frac{\eta_i \cdot T_s}{Q_n}\right) i_k. \qquad (4)$$

Various quantitative definitions for SOP and SOF exist in literature (e.g. Refs. [33–35]), which are all associated with the battery's power capabilities. In this paper, we define SOP as the available source or sink power over a short period of $\Delta t$. Using $V_{OC} = f(SOC)$ as defined in (1), the instantaneous discharge or charge power at time step $k$ can be respectively calculated as,

$$P_{dis,k} = \frac{V_{min}(V_{OC,k} - V_{min})}{\widehat{R}_{eq}} \qquad (5)$$

$$P_{ch,k} = \frac{V_{max}(V_{max} - V_{OC,k})}{\widehat{R}_{eq}} \qquad (6)$$

where $V_{min}$ and $V_{max}$ are the minimum and maximum threshold voltages recommended by the manufacturer for a safe operation and $\widehat{R}_{eq}$ is an estimate for the cell's series-equivalent resistance. To this end, we can define SOF in terms of available power as,

$$SOF = \begin{cases} 1, & \text{for } P_{ch,k} \geq P_{req}^{ch} \text{ and } P_{dis,k} \geq P_{req}^{dis} \\ 0, & \text{for } P_{ch,k} < P_{req}^{ch} \text{ and } P_{dis,k} < P_{req}^{dis} \end{cases} \qquad (7)$$

where $P_{req}^{ch}$ and $P_{req}^{dis}$ are the required quantity of charge or discharge power respectively to complete a particular task. Note that the value of $\widehat{R}_{eq}$ in (5) and (6) can be approximated by applying the Thevenin's Theorem to an equivalent circuit model. Alternatively, the voltage and current waveforms obtained for a sequence of HPPC pulses at every SOC value can be used to calculate a value for the cell's discharge or charge resistance as,

$$R_{dis} = \frac{V_0 - V_1}{I_{dis}}, \quad R_{ch} = \frac{V_3 - V_2}{I_{ch}}. \qquad (8)$$

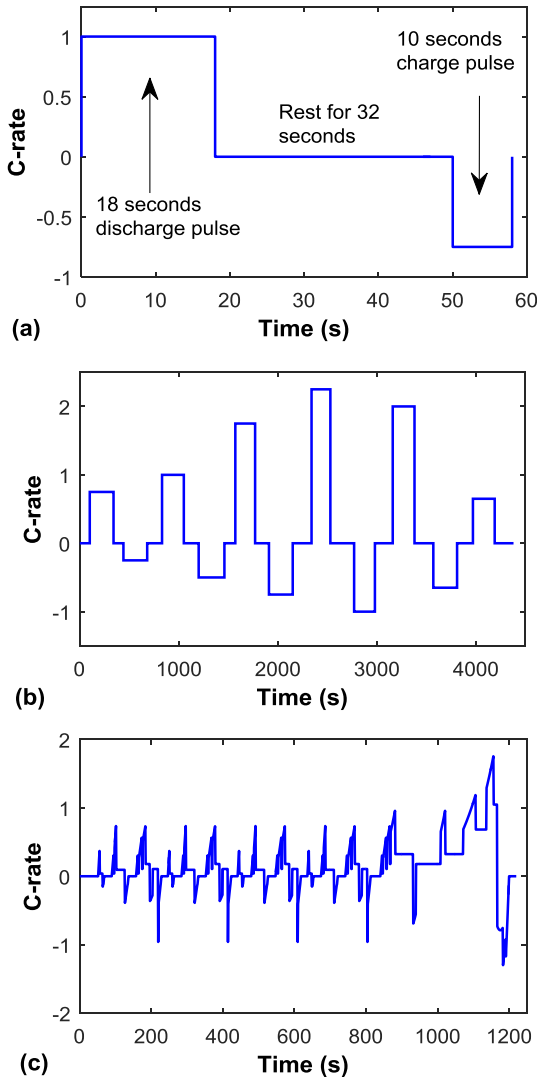In (8), $V_0$ and $V_1$ are the cell voltages measured respectively at the start and end of a discharge current pulse, $I_{dis}$, of duration $\Delta t$ seconds. Similarly, $V_2$ and $V_3$ are the voltage measurements taken for a charge current pulse $I_{ch}$ of duration $\Delta t$ seconds. The resulting resistances are analogous to the cell's internal resistances and can reflect on the power capability of a cell under operation. Consequently, any variations in the cell's internal resistance as a function of SOC and temperature can affect the quality of the SOP estimate at any time.

## 4. Lithium-ion battery models

The candidate battery model structures for the purpose of this review study are summarised in Table 3. These models form the basis for real-time SOC, SOP and SOF estimation algorithms in most lithium-ion battery energy storage applications.

### 4.1. The combined model

The combined model [19] is a very crude approximation of the battery's dynamics. As the name suggests, this model structure is a combination of the Shepherd model [14], Unnewehr and Nasar universal model [36] and the Nernst model [37] given as,

$$V_k = \underbrace{K_0 - \frac{K_1}{SOC_k} - K_2 SOC_k + K_3 \ln(SOC_k) + K_4 \ln(1 - SOC_k)}_{V_{OC} = f(SOC)} - i_k R_s$$

(9)

where $V_k$ is the battery's terminal voltage and $i_k$ is the throughput current. The battery's internal series resistance is described by Ref. $R_s$ and is a function of temperature and SOC. The constants $K_0$, $K_1$, $K_2$, $K_3$ and $K_4$ are used to describe the battery's OCV dependency on SOC. This model benefits from being linear in parameters and thus simplifies the identification procedure.

### 4.2. The rint model

The internal resistance or Rint model is comprised of an ideal voltage source $V_{OC}$ to represent the battery's OCV as a function of SOC and a series resistor $R_s$ that describes the internal ohmic losses [38]. This model structure is also linear in parameters and is very "simple" to implement in real time. However, the model's output equation expressed by (10) is only a crude estimate of the battery's actual terminal voltage, which can result in large uncertainties in SOC and SOP estimates.

$$V_k = V_{OC,k} - i_k R_s.$$

(10)

**Table 3**
Candidate lithium-ion battery models.

| Model | Description |
| --- | --- |
| 1. | Combined model, Eq. (9) |
| 2. | Rint model, Eq. (10) |
| 3. | Huria et al. hysteresis model, Eq. (11) |
| 4. | Plett hysteresis model, Eq. (14) |
| 5. | Randles' model, Eq. (15) |
| 6. | Modified Randles' model, Eq. (17) |
| 7. | One-RC model without hysteresis, Eq. (18) |
| 8. | Two-RC model without hysteresis, Eq. (18) |
| 9. | One-RC model with hysteresis, Eqs. (11) and (18) |
| 10. | Two-RC model with hysteresis, Eqs. (11) and (18) |

### 4.3. The hysteresis models

The OCV as a function of SOC for the two cell chemistries used in this paper are shown in Fig. 3. It is noted that the OCV obtained after a charge step (see Section 2.3) for both LiFePO$_4$ and LiNMC cells has a higher value than that obtained after a discharge step. In literature, this phenomenon is referred to as hysteresis. In Refs. [22], the authors have shown that for high-power LiFePO$_4$ cells, the hysteresis level decreases with increasing rest period allowed immediately after a charge or discharge step. This can be attributed to the thermodynamic origins of the hysteresis effects [39], which requires for a long rest period for the cell to reach an equilibrium potential.

The hysteresis levels obtained after a one-hour rest period for the two cell chemistries under study are presented in Fig. 3(b) and (d). It is apparent that the hysteresis level for the LiFePO$_4$ chemistry is considerably higher than that for the LiNMC chemistry. Moreover, within the useable SOC range of 20%–80%, the OCV curve for the LiFePO$_4$ chemistry is fairly flat. This implies that for those OCV-based SOC estimators, even a small error in the voltage measurement within this region can result in a large deviation from the actual SOC value. Thus, for a more reliable SOC estimation, a model structure of the cell's hysteresis behaviour is of necessity.

To overcome the effect of hysteresis, different modelling approaches have been reported in literature (e.g. Ref. [40]). For those battery chemistries that pose a relatively small hysteresis level (e.g. LiNMC), often a direct approach is adopted [19]. This technique can be achieved either by evaluating the arithmetic mean or minimising the global squared-error between the charge and discharge OCV points obtained separately at the same SOC. However, for those chemistries with larger hysteresis levels (e.g. LiFePO$_4$), the direct methods would lead to large uncertainties in the SOC estimate. Therefore, more comprehensive models are required.

In Refs. [21], the authors develop an empirically-derived hysteresis model for LiFePO$_4$ cells comprising of two parts; first part captures the dynamics of the OCV hysteresis as a function of SOC and an identifiable hysteresis factor that determines the position of the OCV curve with respect to the charge and discharge OCV curves, and the second part considers the SOC-dependent recovery effects (i.e. the time taken for the cell to reach a final equilibrium potential after a current interruption at a given SOC). This results in a comprehensive representation of the cell's OCV during operation. However, due to the empirical nature of the model structure, a training dataset is required to identify the model parameters off-line.

For the purpose of this study, we put the focus on the hysteresis models presented in Refs. [19] and [22] whose parameters can possibly be identified recursively in real time, without the necessity for various training datasets. Another example of on-line OCV hysteresis treatment can be found in Ref. [41]. The first hysteresis model is developed based on an algorithm presented by Huria et al. [22] and is defined as,

$$\nabla V_{OC} = \frac{dV_{OC}}{dSOC} = \begin{cases} \dfrac{dV_{OC,ch}}{dSOC} + m(V_{OC,ch} - V_{OC}), & for \ \dfrac{dSOC}{dt} \geq 0 \\ \dfrac{dV_{OC,dis}}{dSOC} + m(V_{OC,dis} - V_{OC}), & for \ \dfrac{dSOC}{dt} < 0 \end{cases}$$

(11)

which determines the gradient of $V_{OC} = f(SOC)$ as a function of the rate-of-change of SOC and its distance away from the major hysteresis loop formed by the charge,$V_{OC,ch}$, and discharge, $V_{OC,dis}$, OCV curves. The dimensionless coefficient $m$ determines how fast $V_{OC}$ transitions towards $V_{OC,ch}$ or $V_{OC,dis}$ after a preceding charge or
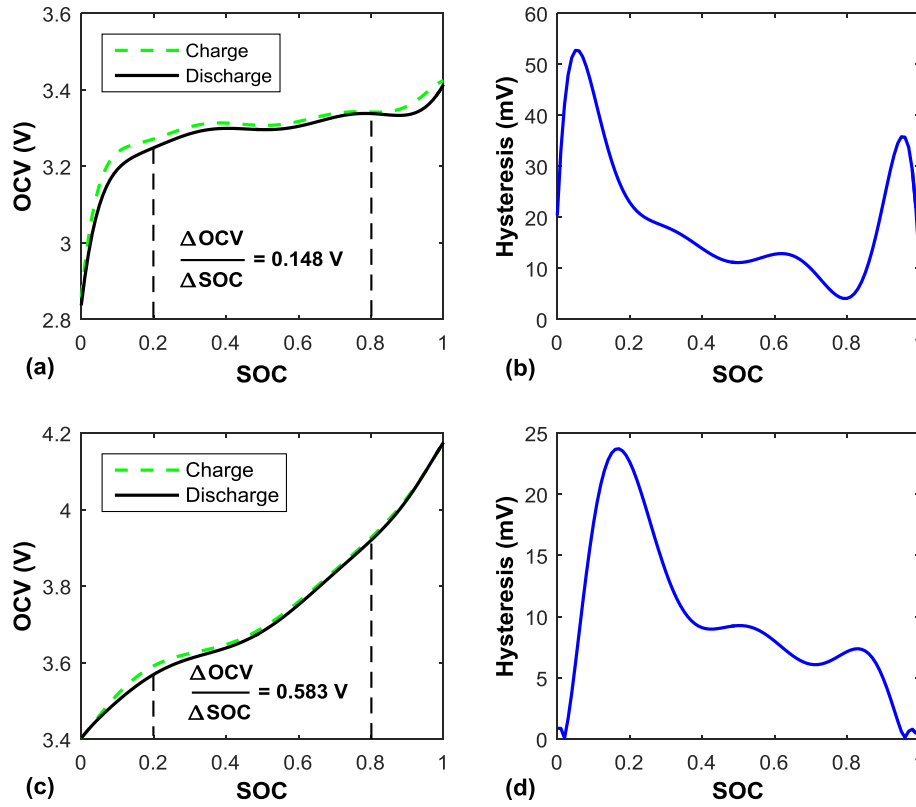
**Fig. 3.** Illustrating open-circuit voltage and hysteresis level for (a)–(b) LiFePO$_4$ and (c)–(d) LiNMC cell chemistries at 25 °C.

discharge current pulse respectively. In order to compare the performance of the two hysteresis models discussed in this section, algorithm (11) is combined with the Rint model (10) to give,

$$V_k = (V_{OC,k} + \nabla V_{OC,k}) - i_k R_s \tag{12}$$

where $\nabla V_{OC,k}$ is the $V_{OC}$ derivative attained at time step $k$.

In Ref. [19] Plett developed a model to describe the hysteresis effects using a differential equation in both time and SOC such as,

$$\frac{dh(SOC,t)}{dSOC} = \gamma \mathrm{sgn}(\dot{SOC})\left(H(SOC,\dot{SOC}) - h(SOC,t)\right) \tag{13}$$

where $h(SOC,t)$ is a function to describe the hysteresis voltage, $H(SOC,\dot{SOC})$ defines the maximum positive and negative hysteresis as a function of SOC and rate-of-change of SOC, $\gamma$ is a tuneable factor to control the rate-of-decay of hysteresis towards the major loop and $\dot{SOC} = dSOC/dt$ is the rate-of-change of SOC. Now, using the definitions given in (1) and (2) and rearranging (13) as a differential equation in time only, the cell model's state-space equations become,

$$h_{k+1} = \exp\left(-\left|\frac{\eta_i i_k \gamma T_s}{Q_n}\right|\right) h_k + \left(1 - \exp\left(-\left|\frac{\eta_i i_k \gamma T_s}{Q_n}\right|\right)\right) H(SOC,\dot{SOC})$$

$$V_k = V_{OC,k} - i_k R_s + h_k. \tag{14}$$

### 4.4. The Randles' model

The Randles' model was originally developed for lead-acid batteries [42–44]. However, in recent years their utilisation in lithium-ion battery modelling has been sighted [45]. Fig. 4(a) shows the Randles' equivalent circuit diagram for a typical lithium-ion cell, where $R_s$ is the series resistance, $R_d$ models the cell's no-load self-discharge (typically ~70k $\Omega$), $C_b$ represents the bulk charge storage of the cell, $C_s$ represents the electrodes' double-layer effect and $R_t$ is the charge-transfer resistance. The voltage $V_{Cb}$ across $C_b$ is analogous to the cell's OCV and the model's output response can be expressed as,

$$\begin{bmatrix} V_{Cb\,k+1} \\ V_{Cs\,k+1} \end{bmatrix} = \begin{bmatrix} e^{\frac{-T_s}{R_d C_b}} & 0 \\ 0 & e^{\frac{-T_s}{R_t C_s}} \end{bmatrix} \begin{bmatrix} V_{Cb\,k} \\ V_{Cs\,k} \end{bmatrix} + \begin{bmatrix} R_d\left(1 - e^{\frac{-T_s}{R_d C_b}}\right) & 0 \\ 0 & R_t\left(1 - e^{\frac{-T_s}{R_t C_s}}\right) \end{bmatrix} i_k \tag{15}$$

$$V_k = V_{Cb,k} - V_{Cs,k} - i_k R_s.$$
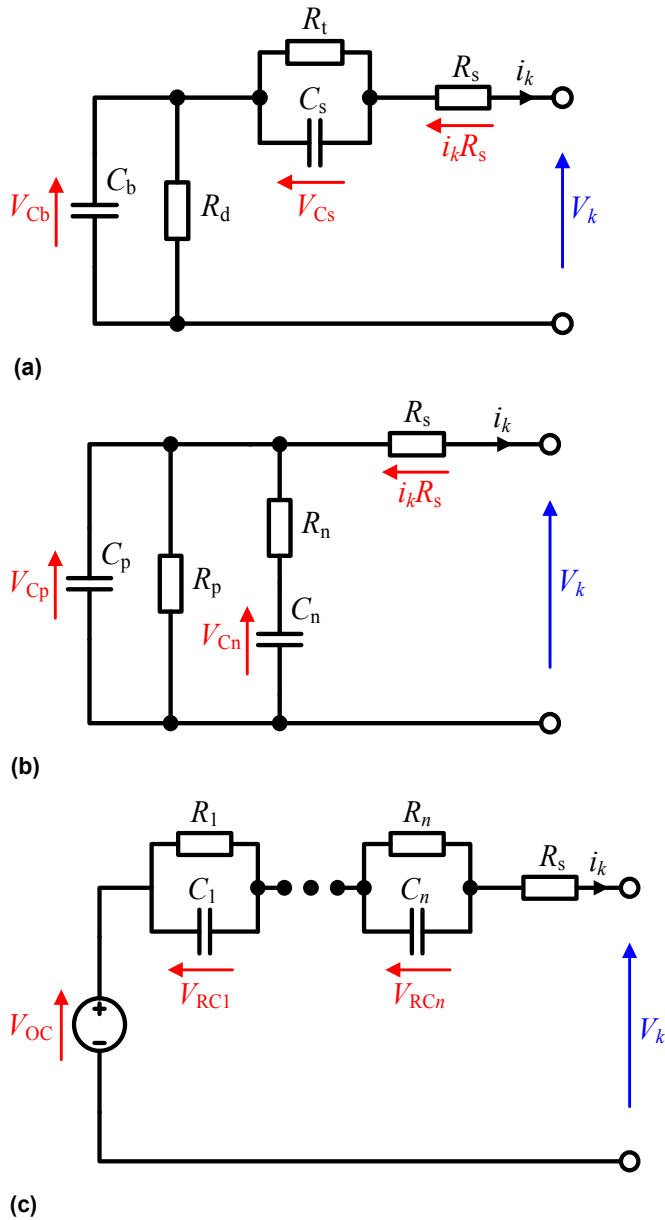
**(a)**



**(b)**



**(c)**

**Fig. 4.** The equivalent ciircuit diagrams for (a) Randles', (b) modified Randles' and (c) $n$-RC model structures.

Gould et al. [28] developed a new battery model through the star-delta transformation of the original Randles' circuit. This particular model, as shown in Fig. 4(b), consists of the same number of parameters as the Randles' model with a slight modification in the way the transient states are represented. In Refs. [28], it is shown that when applied with real-time state observers such as the Utkin and Kalman Filter, the parallel reconfiguration of the Randles' model states can yield a better SOC estimate. Thus, the adaptability of this model structure for online SOC and SOP estimation will be evaluated in this study. Consequently, Mapping the Randles' model parameters as per [28] and solving for the output equation in discrete form yields,

$$
C_n = C_b^2 / (C_b + C_s), \quad C_p = C_p C_s / (C_b + C_s),
$$
$$
R_n = R_t (C_b + C_s)^2 / C_b^2, \quad R_p = R_d + R_t \tag{16}
$$

$$
\begin{bmatrix} V_{Cp\,k+1} \\ V_{Cn\,k+1} \end{bmatrix} = \begin{bmatrix} e^{\frac{-T_s}{\tau_p}} & \frac{R_T}{R_n}\left(1 - e^{\frac{-T_s}{\tau_p}}\right) \\ \left(1 - e^{\frac{-T_s}{\tau_n}}\right) & e^{\frac{-T_s}{\tau_n}} \end{bmatrix} \begin{bmatrix} V_{Cp\,k} \\ V_{Cn\,k} \end{bmatrix}
$$
$$
+ \begin{bmatrix} R_T\left(e^{\frac{-T_s}{\tau_p}} - 1\right) & 0 \\ 0 & 0 \end{bmatrix} i_k V_k = V_{Cp,k} - i_k R_s \tag{17}
$$

where $R_T = R_p R_n / (R_p + R_n)$, $\tau_n = R_n C_n$ and $\tau_p = R_T C_p$.

### 4.5. The RC model

The resistor-capacitor (RC) or the Thevenin equivalent circuit model is a modification of the Rint model, as shown in Fig. 4(c). This model is comprised of an ideal voltage source to represent the cell's OCV at partial equilibrium as a function of SOC, a series ohmic resistance $R_s$ and $n$ number of series-connected RC branches. Depending on the dynamics of the intended application, the number of the RC branches may vary. For most power applications, one RC branch is adequate (e.g. Refs. [46–48]) to describe the long time-constant reactions associated with the diffusion of active species into the electrolyte.

Considering applications with faster transients, the short time-constant reactions associated with the charge-transfer and the double-layer effect of the electrodes can be modelled with additional RC branches (e.g. Refs. [49–52]). However, there is a trade-off between accuracy and complexity, which must be considered for a particular application. In this paper, the performance of one-RC and two-RC models are reviewed analytically. Without loss of generality, the electrical behaviour of an nth order RC model in its discrete form can be expressed as,

$$
\begin{bmatrix} V_{RC1_{k+1}} \\ \vdots \\ V_{RCn_{k+1}} \end{bmatrix} = \begin{bmatrix} e^{\frac{-T_s}{R_1 C_1}} & \cdots & 0 \\ \vdots & \ddots & \vdots \\ 0 & \cdots & e^{\frac{-T_s}{R_n C_n}} \end{bmatrix} \begin{bmatrix} V_{RC1_k} \\ \vdots \\ V_{RCn_k} \end{bmatrix}
$$
$$
+ \begin{bmatrix} R_1\left(1 - e^{\frac{-T_s}{R_1 C_1}}\right) & \cdots & 0 \\ \vdots & \ddots & \vdots \\ 0 & \cdots & R_n\left(1 - e^{\frac{-T_s}{R_n C_n}}\right) \end{bmatrix} i_k V_k
$$
$$
= V_{OC}(SOC_k) - i_k R_s - V_{RC1} - \cdots - V_{RCn}. \tag{18}
$$

## 5. Online non-linear system identification

The Kalman filter is a recursive set of equations that allow for

state estimation and parameter identification of linear time-invariant systems [53]. On the other hand, the EKF is an *ad hoc* solution for the identification of non-linear time-varying systems such that, the non-linear model describing the underlying dynamics of the system is linearised about the filter's current estimated trajectory. For simultaneous estimation of both model states and parameters, two separate are often incorporated in a parallel configuration. This method is referred to in literature as the dual-EKF algorithm [54–57].

Essentially, the dual-EKF combines the state and weight filters, where the model states, including SOC, are estimated by the state filter and the model parameters are identified recursively by the weight filter. Due to its robustness, the Kalman filter algorithm is often utilised in the battery energy and/or power management systems to overcome a wide range of problems (e.g. Refs. [58–61]). Therefore, this popular system identification technique is applied to the candidate battery model structures given in Table 3.

### 5.1. Dual-EKF system identification

With the assumption that the cell terminal current $i_k$ and voltage $V_k$ are the only measurable quantities, the EKF state filter can be designed such that,

$$
\begin{aligned}
\mathbf{x}_{k+1} &= f(\mathbf{x}_k, \mathbf{u}_k, \boldsymbol{\theta}_k) + \mathbf{w}_k \\
\mathbf{y}_k &= h(\mathbf{x}_k, \mathbf{u}_k, \boldsymbol{\theta}_k) + \mathbf{v}_k \\
\mathbf{w}_k &\sim N(0, \mathbf{Q}_k^x) \\
\mathbf{v}_k &\sim N(0, \mathbf{R}_k^x)
\end{aligned}
\tag{19}
$$

where $\mathbf{x}_k \in \mathbb{R}^n$ is a vector containing the model states to be predicted in a minimum variance sense, $\boldsymbol{\theta}_k \in \mathbb{R}^q$ contains the time-varying model parameters, $\mathbf{u}_k \in \mathbb{R}^p$ is the exogenous model input, $\mathbf{y}_k \in \mathbb{R}^m$ is the output and $\mathbf{w}_k \in \mathbb{R}^n$ and $\mathbf{v}_k \in \mathbb{R}^m$ are the zero-mean process and measurement noises of covariance $\mathbf{Q}_k^x$ and $\mathbf{R}_k^x$ respectively. The non-linear function $f(\cdot, \cdot, \cdot)$ relates the states estimated at discrete time $k-1$ to the states at the current time step $k$ and $h(\cdot, \cdot, \cdot)$ maps the updated states to the measurements at time step $k$. Assuming that the parameters vary slowly over time (i.e. minutes to hours), the weight EKF can be designed to adaptively provide an estimate of the true model parameters. Thus, the state-space model for the weight filter is given as,

$$
\begin{aligned}
\boldsymbol{\theta}_{k+1} &= \boldsymbol{\theta}_k + \mathbf{r}_k \\
\mathbf{d}_k &= h(\mathbf{x}_k, \mathbf{u}_k, \boldsymbol{\theta}_k) + \mathbf{e}_k \\
\mathbf{r}_k &\sim N\left(0, \mathbf{Q}_k^\theta\right) \\
\mathbf{e}_k &\sim N\left(0, \mathbf{R}_k^\theta\right)
\end{aligned}
\tag{20}
$$

where the "dynamics" of changes in Ref. $\boldsymbol{\theta}_k$ are attributed to a small "imaginary" white noise $\mathbf{r}_k \in \mathbb{R}^p$ of covariance $\mathbf{Q}_k^\theta$ that evolves the parameters over time. The output equation $\mathbf{d}_k \in \mathbb{R}^m$ is given as a measurable function of $\boldsymbol{\theta}_k$ and a white noise $\mathbf{e}_k \in \mathbb{R}^m$ of covariance $\mathbf{R}_k^\theta$ to account for the sensor noise and modelling uncertainties.

Due to the time-variability of the model parameters, it is imperative that the cell data collected using the current profiles presented in section 2 convey continual information on the parameters to be estimated. This condition is referred to in the system identification literature as the "persistence of excitation" (PE) [62]. In many real-time battery state estimation problems, the load-current profile may not fully satisfy the PE criterion. For those observer-based SOC estimators such as the extended Luenberger observer, sliding mode or adaptive observers, if the PE condition is not sufficiently satisfied, the gains tend to approach infinity and divergence occurs [62]. Nevertheless, the EKF algorithm seems to operate well under such conditions without any divergence (e.g.

Refs. [63–66]). This is due to the presence of the persistently exciting process and measurement noise, which are assumed to be white colour for the dual-EKF estimator presented here. Note that white noise has a continuous spectrum over the whole frequency range and thus is persistently exciting for any finite order [67,68].

For brevity, a summary of the dual-EKF algorithm is presented in Table 4. Note that the algorithm is initialised by assuming a prior knowledge of the model states and parameters are available. However, in practice the initial system information are unknown. Thus, the states and the parameters are set to their best guess values at $k = 0$ so that $\widehat{\boldsymbol{\theta}}_0^+ = E[\boldsymbol{\theta}_0]$ and $\widehat{\mathbf{x}}_0^+ = E[\mathbf{x}_0]$. The estimation error covariance matrices are also initialised as $\mathbf{P}_{\theta,0}^+ = E[(\boldsymbol{\theta} - \widehat{\boldsymbol{\theta}}_0^+)(\boldsymbol{\theta} - \widehat{\boldsymbol{\theta}}_0^+)^T]$ and $\mathbf{P}_{x,0}^+ = E[(\mathbf{x} - \widehat{\mathbf{x}}_0^+)(\mathbf{x} - \widehat{\mathbf{x}}_0^+)^T]$.

Each time step, the algorithm first updates the state and parameter estimates $\widehat{\mathbf{x}}_k^-$ and $\widehat{\boldsymbol{\theta}}_k^-$ and their error covariance $\mathbf{P}_{\tilde{x},k}^-$ and $\mathbf{P}_{\tilde{\theta},k}^-$ respectively, by propagating them forward in time. Note that for the parameter time-update equation (25), the new parameter estimate $\widehat{\boldsymbol{\theta}}_k^-$ is equal to the previous estimate $\widehat{\boldsymbol{\theta}}_{k-1}^+$ with an increase in its uncertainty due to the presence of the white process noise $\mathbf{r}_k$. After a measurement has been taken at time step $k$, both filters take this measurement into consideration to update the state and parameter estimates $\widehat{\mathbf{x}}_k^+$ and $\widehat{\boldsymbol{\theta}}_k^+$ and their corresponding uncertainties as $\mathbf{P}_{\tilde{x},k}^+$ and $\mathbf{P}_{\tilde{\theta},k}^+$ respectively. In (26) and (27), the measurement-update error covariance matrices $\mathbf{P}_{\tilde{x},k}^+$ and $\mathbf{P}_{\tilde{\theta},k}^+$ are given in their Joseph forms to ensure a numerically robust algorithm.

It is noted that for the weight filter's measurement-update equations given in (27), the total-differential $\mathbf{H}_k^\theta$ of the model output equation $h(\cdot, \cdot, \cdot)$ with respect to parameters $\boldsymbol{\theta}_k$ is required. Therefore, by decomposing the total-derivative into partial-derivatives, $\mathbf{H}_k^\theta$ is computed recursively as the following set of equations,

$$
\mathbf{H}_k^\theta = \left. \frac{dh\left(\widehat{\mathbf{x}}_k^-, \mathbf{u}_k, \boldsymbol{\theta}_k\right)}{d\boldsymbol{\theta}_k} \right|_{\boldsymbol{\theta}_k = \widehat{\boldsymbol{\theta}}_k^-}
$$

$$
\frac{dh\left(\widehat{\mathbf{x}}_k^-, \mathbf{u}_k, \widehat{\boldsymbol{\theta}}_k^-\right)}{d\widehat{\boldsymbol{\theta}}_k^-} = \frac{\partial h\left(\widehat{\mathbf{x}}_k^-, \mathbf{u}_k, \widehat{\boldsymbol{\theta}}_k^-\right)}{\partial \widehat{\boldsymbol{\theta}}_k^-} + \frac{\partial h\left(\widehat{\mathbf{x}}_k^-, \mathbf{u}_k, \widehat{\boldsymbol{\theta}}_k^-\right)}{\partial \widehat{\mathbf{x}}_k^-} \cdot \frac{d\widehat{\mathbf{x}}_k^-}{d\widehat{\boldsymbol{\theta}}_k^-}
$$

$$
\frac{d\widehat{\mathbf{x}}_k^-}{d\widehat{\boldsymbol{\theta}}_k^-} = \frac{\partial f\left(\widehat{\mathbf{x}}_{k-1}^+, \mathbf{u}_{k-1}, \widehat{\boldsymbol{\theta}}_k^-\right)}{\partial \widehat{\boldsymbol{\theta}}_k^-} + \frac{\partial f\left(\widehat{\mathbf{x}}_{k-1}^+, \mathbf{u}_{k-1}, \widehat{\boldsymbol{\theta}}_k^-\right)}{\partial \widehat{\mathbf{x}}_{k-1}^+} \cdot \frac{d\widehat{\mathbf{x}}_{k-1}^+}{d\widehat{\boldsymbol{\theta}}_k^-}
$$

$$
\frac{d\widehat{\mathbf{x}}_{k-1}^+}{d\widehat{\boldsymbol{\theta}}_k^-} = \frac{d\widehat{\mathbf{x}}_{k-1}^-}{d\widehat{\boldsymbol{\theta}}_{k-1}^+} - \mathbf{L}_{k-1}^x \frac{dh\left(\widehat{\mathbf{x}}_{k-1}^-, \mathbf{u}_{k-1}, \widehat{\boldsymbol{\theta}}_{k-1}^+\right)}{d\widehat{\boldsymbol{\theta}}_{k-1}^+}.
\tag{21}
$$

Since $\mathbf{L}_{k-1}^x$ is weakly related to the parameter estimates $\boldsymbol{\theta}_k$, it can be safely neglected in (21) to improve the efficiency of the weight filter. Furthermore, $d\widehat{\mathbf{x}}_{k-1}^+/d\widehat{\boldsymbol{\theta}}_k^-$ is set to zero at $k = 0$ and the three total-derivatives are updated recursively. In order to ensure the convergence of the state and weight filers, it is important to tune the error covariance matrices. In this case, the tuning variables are $\mathbf{Q}_k^x$, $\mathbf{P}_{\tilde{x},k}^+$ and $\mathbf{R}_0^x$ matrices for the state filter and $\mathbf{Q}_k^\theta$, $\mathbf{P}_{\tilde{\theta},k}^+$ and $\mathbf{R}_k^\theta$ matrices for the weight filter. At time step $k = 0$, these parameters are initialised as,

$$
\begin{aligned}
\mathbf{Q}_0^x &= \text{diag}_n\left\{1 \times 10^{-6}\right\}, & \mathbf{P}_{\tilde{x},0}^+ &= \text{diag}_n\{10\}, & \mathbf{R}_0^x &= \text{diag}_m\{10\} \\
\mathbf{Q}_0^\theta &= \text{diag}_q\left\{1 \times 10^{-8}\right\}, & \mathbf{P}_{\tilde{\theta},0}^+ &= \text{diag}_q\{10\}, & \mathbf{R}_0^\theta &= \text{diag}_m\{10\}
\end{aligned}
\tag{22}
$$

where diag$\{\cdot\}$ is a diagonal matrix of size $n \times n$ for $\mathbf{Q}_0^x$ and $\mathbf{P}_{\tilde{x},0}^+$, $q \times q$

**Table 4**
Summary of the Dual-EKF algorithm for battery model state and parameter estimation.

Initialisation:

$$\widehat{\boldsymbol{\theta}}_0^+ = E[\boldsymbol{\theta}_0], \quad \mathbf{P}_{\theta,0}^+ = E\left[\left(\boldsymbol{\theta} - \widehat{\boldsymbol{\theta}}_0^+\right)\left(\boldsymbol{\theta} - \widehat{\boldsymbol{\theta}}_0^+\right)^T\right]$$

$$\widehat{\mathbf{x}}_0^+ = E[\mathbf{x}_0], \quad \mathbf{P}_{x,0}^+ = E\left[\left(\mathbf{x} - \widehat{\mathbf{x}}_0^+\right)\left(\mathbf{x} - \widehat{\mathbf{x}}_0^+\right)^T\right]$$

(23)

Time-update equations for state filter:

$$\widehat{\mathbf{x}}_k^- = f\left(\widehat{\mathbf{x}}_{k-1}^+, \mathbf{u}_{k-1}, \widehat{\boldsymbol{\theta}}_k^-\right)$$

$$\mathbf{P}_{\tilde{x},k}^- = \mathbf{F}_{k-1}\mathbf{P}_{\tilde{x},k-1}^+\mathbf{F}_{k-1}^T + \mathbf{Q}_k^x$$

(24)

Time-update equations for weight filter:

$$\widehat{\boldsymbol{\theta}}_k^- = \widehat{\boldsymbol{\theta}}_{k-1}^+$$

$$\mathbf{P}_{\tilde{\theta},k}^- = \mathbf{P}_{\tilde{\theta},k-1}^+ + \mathbf{Q}_k^\theta$$

(25)

Measurement-update equations for state filter:

$$\mathbf{L}_k^x = \mathbf{P}_{\tilde{x},k}^-(\mathbf{H}_k^x)^T\left[\mathbf{H}_k^x\mathbf{P}_{\tilde{x},k}^-(\mathbf{H}_k^x)^T + \mathbf{R}_k^x\right]^{-1}$$

$$\widehat{\mathbf{x}}_k^+ = \widehat{\mathbf{x}}_k^- + \mathbf{L}_k^x\left[\mathbf{y}_k - h\left(\widehat{\mathbf{x}}_k^-, \mathbf{u}_k, \widehat{\boldsymbol{\theta}}_k^-\right)\right]$$

$$\mathbf{P}_{\tilde{x},k}^+ = (\mathbf{I} - \mathbf{L}_k^x\mathbf{H}_k^x)\mathbf{P}_{\tilde{x},k}^-(\mathbf{I} - \mathbf{L}_k^x\mathbf{H}_k^x)^T + \mathbf{L}_k^x\mathbf{R}_k^x(\mathbf{L}_k^x)^T$$

(26)

Measurement-update equations for weight filter:

$$\mathbf{L}_k^\theta = \mathbf{P}_{\tilde{\theta},k}^-\left(\mathbf{H}_k^\theta\right)^T\left[\mathbf{H}_k^\theta\mathbf{P}_{\tilde{\theta},k}^-\left(\mathbf{H}_k^\theta\right)^T + \mathbf{R}_k^\theta\right]^{-1}$$

$$\widehat{\boldsymbol{\theta}}_k^+ = \widehat{\boldsymbol{\theta}}_k^- + \mathbf{L}_k^\theta\left[\mathbf{d}_k - h\left(\widehat{\mathbf{x}}_k^-, \mathbf{u}_k, \widehat{\boldsymbol{\theta}}_k^-\right)\right]$$

$$\mathbf{P}_{\tilde{\theta},k}^+ = \left(\mathbf{I} - \mathbf{L}_k^\theta\mathbf{H}_k^\theta\right)\mathbf{P}_{\tilde{\theta},k}^-\left(\mathbf{I} - \mathbf{L}_k^\theta\mathbf{H}_k^\theta\right)^T + \mathbf{L}_k^\theta\mathbf{R}_k^\theta\left(\mathbf{L}_k^\theta\right)^T$$

(27)

where,

$$\mathbf{F}_{k-1} = \left.\frac{\partial f\left(\mathbf{x}_{k-1}, \mathbf{u}_{k-1}, \widehat{\boldsymbol{\theta}}_k^-\right)}{\partial \mathbf{x}_{k-1}}\right|_{\mathbf{x}_{k-1}=\widehat{\mathbf{x}}_{k-1}^+}, \quad \mathbf{H}_k^x = \left.\frac{\partial h\left(\mathbf{x}_k, \mathbf{u}_k, \widehat{\boldsymbol{\theta}}_k^-\right)}{\partial \mathbf{x}_k}\right|_{\mathbf{x}_k=\widehat{\mathbf{x}}_k^-}, \quad \mathbf{H}_k^\theta = \left.\frac{dh\left(\widehat{\mathbf{x}}_k^-, \mathbf{u}_k, \boldsymbol{\theta}_k\right)}{d\boldsymbol{\theta}_k}\right|_{\boldsymbol{\theta}_k=\widehat{\boldsymbol{\theta}}_k^-}.$$

(28)

for $\mathbf{Q}_0^\theta$ and $\mathbf{P}_{\tilde{\theta},0}^+$ and $m \times m$ for $\mathbf{R}_0^x$ and $\mathbf{R}_0^\theta$ matrices respectively.

## 6. Results and discussion

A statistical analysis of the test results was performed. Fig. 5 presents the average root-mean-squared-error (RMSE) voltage for each set of LiFePO$_4$ and LiNMC cells for the self-designed pulse test results. In order to mitigate the SOC dependency of the OCV functions, the true SOC values obtained using the coulomb-counting technique were used to compute the RMSE values for each model structure. It is evident that the Rint model has the largest error for both lithium-ion cell chemistries. This is due to the absence of any transient states as to capture the underlying dynamics of the electrochemical and thermodynamic processes.

The hysteresis models perform consistently better compared to the simple Rint model. This improvement is attributed to the fact that there exists a hysteresis level for both LiFePO$_4$ and LiNMC cell chemistries, which needs considering for more accurate cell modelling. Although similar results are achieved by the two hysteresis models (3 and 4), the model structure proposed by Huria et al. [22] is comparatively more favourable in real-time applications as it only has one identifiable parameter. This further reduces the computational burden on the BMS. The Randles' and the modified Randles' models both have two capacitors to include the OCV and the transients associated with the diffusion effects respectively. However, a large error is induced due to the instabilities in the battery model states.

Compared to other structures, the one- and two-RC models both demonstrate excellent modelling capabilities. These two models have a separate empirical function as to describe the cell's OCV as a function of SOC. It is observable that by including the OCV hysteresis as one of the EKF states, an even better modelling result in terms of RMSE is achievable.

In order to study the SOC estimation and tracking capability of each model structure, the results for the multi-cycle NEDC test over the SOC range of 5–90% were used. The dual-EKF algorithm was initialised with the best-guess values for the model parameters and the SOC state was set to its true value. Fig. 6 presents the estimated cell voltage for one NEDC cycle at SOC = 64% for one of the LiFePO$_4$ test cells. The results obtained for the LiNMC cells pose a similar behaviour. It can be noted that the two-RC model structure with hysteresis included has the closest fit to the true cell voltage.

Fig. 7 illustrates the resulting model-based SOC estimation errors at five different temperature settings. The average SOC errors for the three LiFePO$_4$ set of cells are shown in Fig. 7(a) and those for the LiNMC set of cells are shown in Fig. 7(b). The EKF SOC state for all models was correctly initialised to 90% and the filter and hysteresis states were set to zero. It can be noted that at low operating temperatures, the induced SOC error is the largest. This is due to the fact that at low temperatures, the inherent electrochemical reactions are significantly slower. Thus, it becomes more difficult to model the underlying cell dynamics, leading to a larger modelling and SOC error.

The average SOC errors in Fig. 7 show that, the one- and two-RC model structures pose a considerably better performance for SOC estimation in real time for both cell chemistries. This can be attributed to the enhanced characterisation of the charge-transfer and diffusion effects by the model states. Moreover, by including the hysteresis effects in the RC-network model structures, a further improvement in the SOC estimate can be achieved.

Thus far, the SOC estimation results presented have been obtained using correct initialisation for the EKF's SOC state. In practice, the EKF would be initialised with a "best" estimate for SOC, which is usually realised based on OCV measurements prior to a load connection and/or using the cell's most recent history of usage. Either way results in an inaccurate *a priori* estimate for the SOC
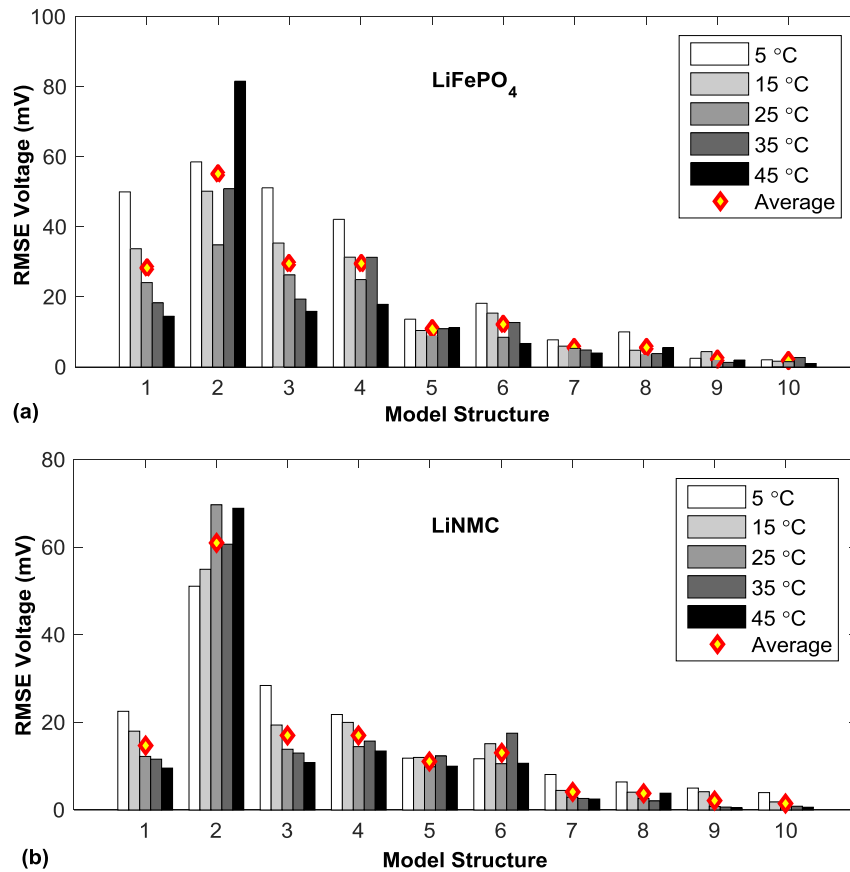
**Fig. 5.** Average modelling error for the self-designed pulse test for (a) LiFePO$_4$ and (b) LiNMC set of cells over the temperature range 5−45 °C.
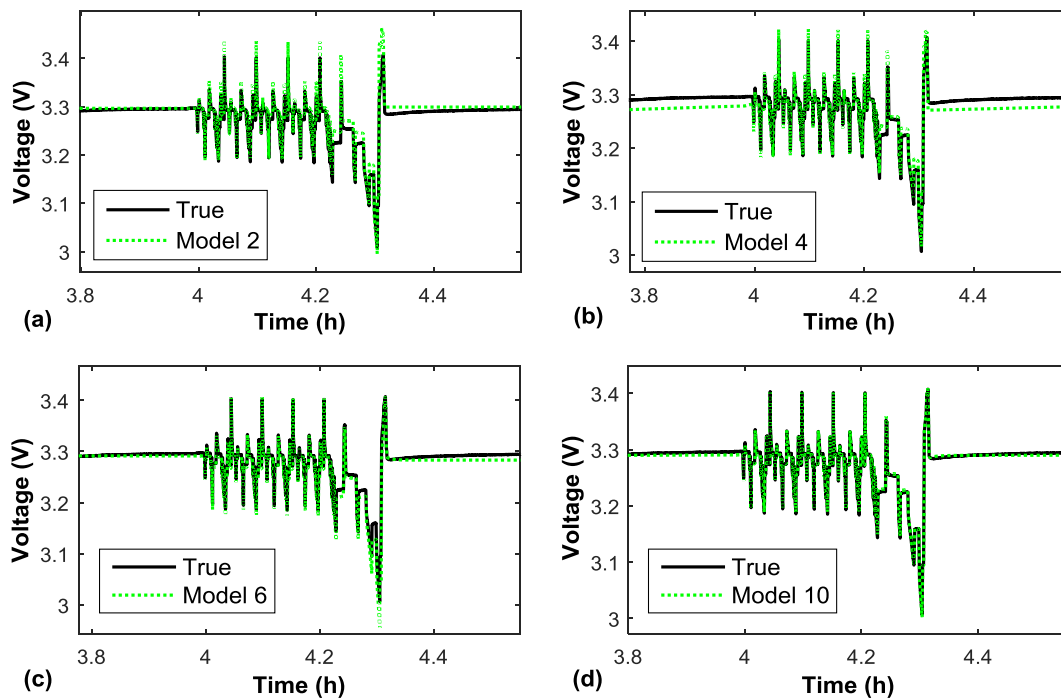


**Fig. 6.** Estimated voltage from one NEDC cycle for (a) the Rint, (b) the One-state Hysteresis, (c) the modified Randles' and (d) the Two-RC model with hysteresis for a LiFePO$_4$ cell at 25 °C.
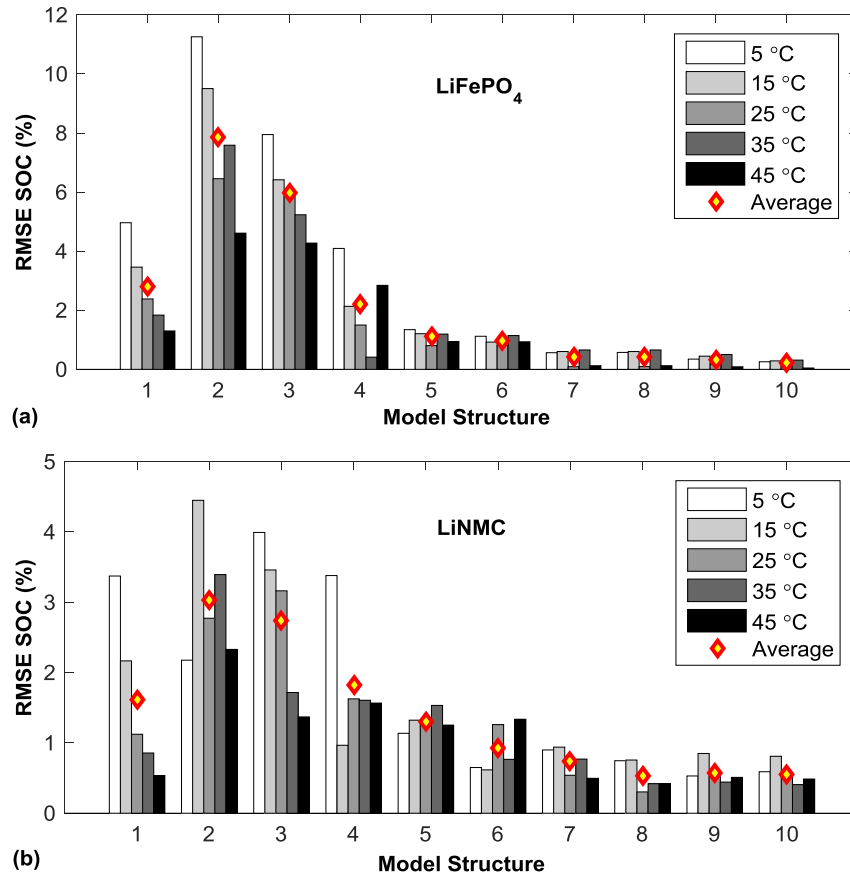
**Fig. 7.** Average SOC estimation error for the multi-cycle NEDC test for (a) LiFePO₄ and (b) LiNMC set of cells over the temperature range 5–45 °C.

state, which can be exacerbated if the measured OCV lies within the flat region of operation for the LiFePO₄ chemistry or the cell has not rested long enough.

Therefore, we may now extend our investigation by comparing the estimation results attainable using incorrect EKF initialisation for the ten model structures.

Using the measurements recorded for the pulsed-current test profile (see Fig. 2(b)) at 25 °C, SOC was estimated for all the LiFePO₄ and LiNMC test cells under three different EKF initialisation scenarios. Firstly, the SOC state was correctly initialised to 100% and the results are presented in Table 5. As can be seen, all the model structures are able to achieve a SOC estimate that is within the standard ±5% error bound, given correct initialisation of the SOC state. Secondly, the SOC state was incorrectly initialised to 80% instead of 100%. The results are presented in Table 6. It is evident

that compared to other model structures, both RC models with and without the hysteresis included achieved outstanding SOC estimation errors. Finally, the SOC state was incorrectly set to 60% instead of 100%. Similar results are obtainable as presented in Table 7. It should be noted that the SOC error statistics for the three SOC initialisation cases given here were computed by excluding the first hour of the SOC data. This allowed for a reasonable convergence towards the "actual" SOC for all the model structures.

As presented in Tables 6 and 7, the best SOC estimation results with incorrectly initialised filter states are realised with the hysteresis model 3 and the one- and two-RC models 7 and 8 respectively. It is apparent that containing the transient effects in a cell model not only improves the characterisation of a cell under load conditions in real time (see Fig. 5), but also results in a more robust SOC estimator. Furthermore, to reduce the uncertainties in the SOC

**Table 5**
SOC estimation results for the pulsed-current test profile at 25 °C with correct initialisation of 100%.

| Model | LiFePO₄ | | | LiNMC | | |
|---|---|---|---|---|---|---|
| | Average error (%) | Maximum error (%) | Standard deviation of error | Average error (%) | Maximum error (%) | Standard deviation of error |
| 1. | 3.93 | 5.27 | 1.53e−4 | 5.24 | 6.80 | 1.46e−3 |
| 2. | 2.13 | 9.63 | 1.94e−3 | 3.09 | 11.11 | 6.08e−3 |
| 3. | 3.17 | 14.35 | 1.10e−3 | 2.80 | 9.78 | 7.77e−3 |
| 4. | 2.73 | 8.93 | 3.22e−3 | 4.95 | 14.76 | 1.46e−2 |
| 5. | 3.88 | 5.86 | 2.61e−3 | 6.47 | 16.32 | 3.78e−3 |
| 6. | 3.03 | 6.02 | 7.21e−4 | 2.20 | 5.21 | 8.43e−3 |
| 7. | 2.66 | 10.74 | 1.05e−3 | 2.15 | 7.98 | 5.95e−3 |
| 8. | 2.65 | 10.64 | 1.06e−3 | 2.15 | 7.78 | 5.99e−3 |
| 9. | 1.39 | 8.58 | 6.56e−4 | 2.89 | 9.69 | 6.55e−3 |
| 10. | 1.44 | 6.78 | 1.35e−3 | 2.15 | 7.96 | 5.99e−3 |

**Table 6**
SOC estimation results for the pulsed-current test profile at 25 °C with incorrect initialisation of 80% when actual SOC = 100%.

| Model | LiFePO$_4$ | | | LiNMC | | |
|---|---|---|---|---|---|---|
| | Average error (%) | Maximum error (%) | Standard deviation of error | Average error (%) | Maximum error (%) | Standard deviation of error |
| 1. | 13.19 | 14.82 | 5.6e−4 | 5.23 | 7.17 | 2.06e−3 |
| 2. | 6.33 | 11.39 | 6.5e−3 | 3.09 | 10.91 | 4.2e−3 |
| 3. | 3.40 | 14.65 | 1.6e−3 | 2.80 | 9.79 | 6.2e−3 |
| 4. | 6.96 | 13.67 | 1.1e−2 | 4.95 | 16.16 | 1.0e−2 |
| 5. | 3.62 | 6.47 | 3.5e−3 | 6.47 | 15.72 | 3.41e−3 |
| 6. | 5.07 | 9.46 | 2.9e−4 | 2.20 | 6.79 | 2.70e−3 |
| 7. | 3.03 | 11.18 | 8.5e−4 | 2.15 | 8.03 | 5.16e−3 |
| 8. | 3.02 | 11.06 | 9.0e−4 | 2.14 | 8.01 | 5.16e−3 |
| 9. | 2.28 | 11.03 | 6.8e−4 | 2.89 | 9.69 | 7.05e−3 |
| 10. | 2.01 | 8.37 | 1.4e−−3 | 2.15 | 8.01 | 5.11e−3 |

**Table 7**
SOC estimation results for the pulsed-current test profile at 25 °C with incorrect initialisation of 60% when actual SOC = 100%.

| Model | LiFePO$_4$ | | | LiNMC | | |
|---|---|---|---|---|---|---|
| | Average error (%) | Maximum error (%) | Standard deviation of error | Average error (%) | Maximum error (%) | Standard deviation of error |
| 1. | 13.45 | 14.82 | 4.57e−3 | 10.00 | 10.78 | 1.05e−3 |
| 2. | 19.58 | 35.74 | 6.24e−4 | 3.54 | 10.94 | 2.97e−3 |
| 3. | 3.72 | 14.70 | 2.35e−3 | 3.27 | 9.80 | 5.28e−3 |
| 4. | 16.20 | 31.63 | 2.86e−3 | 6.56 | 16.52 | 1.03e−2 |
| 5. | 8.61 | 16.98 | 2.87e−3 | 6.60 | 15.98 | 3.15e−3 |
| 6. | 11.42 | 21.17 | 4.93e−4 | 2.55 | 5.97 | 1.95e−3 |
| 7. | 3.12 | 11.25 | 8.50e−4 | 2.33 | 8.07 | 4.55e−3 |
| 8. | 3.12 | 11.12 | 8.50e−4 | 2.32 | 8.05 | 4.50e−3 |
| 9. | 2.47 | 11.17 | 3.21e−4 | 2.78 | 9.69 | 7.35e−3 |
| 10. | 2.34 | 8.80 | 5.69e−4 | 2.34 | 8.06 | 4.40e−3 |
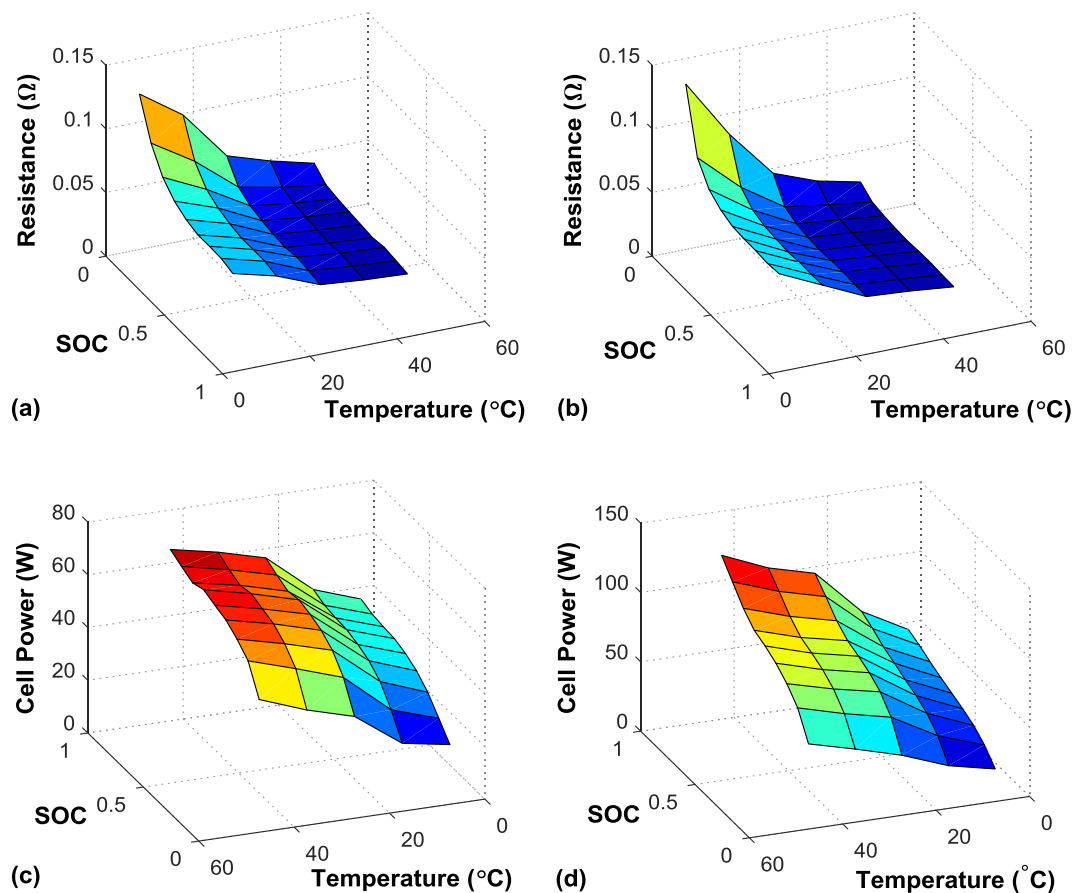


**Fig. 8.** Comparison of (a) and (b) internal series resistances and (c) and (d) calculated discharge power using the HPPC method for the LiFePO$_4$ and LiNMC cells as a function of SOC and temperature.

**Table 8**
Comparison of the EKF identified equivalent cell resistance with that calculated for the LiFePO$_4$ and LiNMC cells for a single HPPC repetition at 25 °C and SOC = 90%.

| Model | LiFePO$_4$ | | LiNMC | |
|---|---|---|---|---|
| | EKF identified $R_{eq}$ (m$\Omega$) | Mean error (m$\Omega$) | EKF identified $R_{eq}$ (m$\Omega$) | Mean error (m$\Omega$) |
| 1. | 35.5 | 8.1 | 26.5 | 7.8 |
| 2. | 38.4 | 5.2 | 28.3 | 6.0 |
| 3. | 45.6 | 2.0 | 46.4 | 12.1 |
| 4. | 38.4 | 5.2 | 28.3 | 6.0 |
| 5. | 37.9 | 5.7 | 29.4 | 4.9 |
| 6. | 36.4 | 7.2 | 27.8 | 6.5 |
| 7. | 48.2 | 4.6 | 29.5 | 4.8 |
| 8. | 47.0 | 3.4 | 30.2 | 4.1 |
| 9. | 46.0 | 2.4 | 32.7 | 1.6 |
| 10. | 47.3 | 3.7 | 36.6 | 2.3 |

**Table 9**
Comparison of identified model parameters for 2-RC model structure using the precise EIS method against the EKF parameters identification method at SOC = 20%.

| 2-RC model parameter | EIS identified | EKF identified | Absolute error |
|---|---|---|---|
| $R_s$ (m$\Omega$) | 25.47 | 25.55 | 0.08 |
| $R_1$ (m$\Omega$) | 13.30 | 10.35 | 2.95 |
| $C_1$ (F) | 1424 | 1561 | 137 |
| $R_2$ (m$\Omega$) | 13.83 | 12.41 | 1.42 |
| $C_2$ (F) | 6.2 | 6.8 | 0.60 |

estimate, the hysteresis functions can possibly be merged with the RC models resulting in a better SOC convergence.

Using the HPPC method [32], the cell discharge resistance and power for every LiFePO$_4$ and LiNMC test cell under a current pulse with duration of 18 s, over a SOC range of 10—90% at five different operating temperatures is calculated. The averaged-results for the two sets of chemistries are presented in Fig. 8. Whereas Fig. 8(a) and (b) demonstrate the variation of the discharge cell resistance calculated using (8), Fig. 8(c) and (d) display how the quantity of available discharge power for a fixed current pulse duration may vary with respect to SOC and temperature for the LiFePO$_4$ and LiNMC cells respectively. It can be noted that at high temperature and SOC values, the cell resistance is smallest for both chemistries, resulting in a larger quantity of power being available for discharge. Moreover, at high SOC values, the corresponding OCV is also larger, which further improves the cell's capability to source power, without violating the safe operating voltage thresholds.

As defined by (5) and (6), the quality of the estimated instantaneous discharge or charge power largely depends on the accuracy of the identified cell resistance under various operating scenarios. Using the EKF-identified model parameters obtained for each test cell under a single HPPC repetition at 25 °C and SOC = 90%, the Thevenin equivalent circuit resistance, $R_{eq}$, for every model structure presented in this paper is calculated. The obtained model-based cell resistances for each set of chemistries are then averaged and compared to the average of the charge and discharge resistances given by (8) for the same HPPC profile. The results are presented in Table 8. It is evident that the two-RC model and the one-RC with adaptive hysteresis model provide the best estimates

**Table 10**
Comparison of identified model parameters for 2-RC model structure using the precise EIS method against the EKF parameters identification method at SOC = 80%.

| 2-RC model parameter | EIS identified | EKF identified | Absolute error |
|---|---|---|---|
| $R_s$ (m$\Omega$) | 24.02 | 24.09 | 0.07 |
| $R_1$ (m$\Omega$) | 13.63 | 13.92 | 0.29 |
| $C_1$ (F) | 1355 | 1293 | 62 |
| $R_2$ (m$\Omega$) | 9.39 | 9.64 | 0.25 |
| $C_2$ (F) | 5.9 | 5.8 | 0.10 |

for the cell's equivalent resistance, which can be used to improve the quality of the model-based SOP estimate. Additionally, the EKF identified $R_{eq}$ parameter for SOP predictions is shown to have a very low mean error for all model structures.

The electrochemical impedance spectroscopy (EIS) is a widely used experimental technique for accurate identification of battery model parameters [31]. Thus, in this paper, to further demonstrate the reliability of the dual-EKF algorithm, the EIS method is implemented as per [49] in order to identify the 2-RC model parameters for one LiNMC test cell as a function of SOC. The results are compared against those attained using the dual-EKF algorithm at SOC steps of 20 and 80% and are presented in Table 9 and Table 10 respectively. It is apparent that despite the lack of persistent excitation of the NEDC current profile, the EKF algorithm is capable of tracking the SOC-dependent variations in the battery model parameters. This is true if and only if a reasonable prior knowledge of the model parameters is available. Otherwise, the input signal is required to completely satisfy the persistent excitation condition [69].

Note that for a reliable SOP assessment, an accurate SOC estimate is also required, which in turn reflects on the accuracy of the cell's predicted OCV in (5) and (6). Thus, to this end, the two-RC model structure can be nominated as an optimum selection with only two estimable states and five identifiable parameters for superior cell dynamic modelling and joint SOC and SOP estimation results. Alternatively, for cell chemistries with large inherent hysteresis levels, the one-RC with hysteresis model is preferred.

## 7. Conclusion

This paper has systematically reviewed the most common lumped-parameter equivalent circuit models used in lithium-ion battery energy storage applications based on their number of appearances in literature. The merits for comparison were modelling accuracy in terms of average root-mean-squared-error for two sets of lithium-ion cells of different electrode chemistries, namely the LiFePO$_4$ and LiNMC. The generality of each model structure was examined over a temperature range of 5—45 °C. The battery models' parameters and states were recursively estimated using a nonlinear system identification technique based on the dual-EKF algorithm. Furthermore, the dynamic performance of each model structure for joint estimation of SOC and SOP were discussed. The results suggested that the two-RC model structure, with two estimable states and five identifiable parameters, is an optimum choice for implementation of most battery energy and power management strategies. Alternatively, for cell chemistries with large inherent hysteresis levels, the one-RC model with hysteresis included is preferred without an increase in complexity.

## Acknowledgement

## References

[1] H. Rahimi-Eichi, U. Ojha, F. Baronti, M. Chow, Ind. Electron. Mag. IEEE 7 (2013) 4–16.
[2] T. Kim, Y. Wang, H. Fang, Z. Sahinoglu, T. Wada, S. Hara, W. Qiao, J. Power Sources 295 (2015) 16–27.
[3] W. Waag, C. Fleischer, D.U. Sauer, J. Power Sources 258 (2014) 321–339.
[4] L. Lu, X. Han, J. Li, J. Hua, M. Ouyang, J. Power Sources 226 (2013) 272–288.
[5] S. Jung, J. Power Sources 264 (2014) 184–194.
[6] A. Khandelwal, K.S. Hariharan, V.S. Kumar, P. Gambhire, S.M. Kolake, D. Oh, S. Doo, J. Power Sources 248 (2014) 101–114.
[7] N.A. Chaturvedi, R. Klein, (2010) 1997–2002.
[8] K. Smith, Control Syst. IEEE 30 (2) (2010) 18–25.
[9] J. Marcicki, A.T. Conlisk, G. Rizzoni, J. Power Sources 251 (2014) 157–169.
[10] G.K. Prasad, C.D. Rahn, J. Dyn, Syst. Meas. Control 136 (2014) 041012.
[11] J.L. Lee, L.L. Aldrich, K.D. Stetzel, G.L. Plett, J. Power Sources 255 (2014) 85–100.
[12] C. Speltino, D. Di Domenico, G. Fiengo, a. Stefanopoulou, in: Proc. 48h IEEE Conf. Decis. Control Held Jointly with 2009 28th Chinese Control Conf, 2009, pp. 3276–3281.
[13] C.M. Shepherd, J. Electrochem. Soc. 112 (1965) 657–664.
[14] S. Li, B. Ke, IEEE Power Energy Soc. Gen. Meet. (2011) 1–8.
[15] O. Tremblay, M. Ieee, L. Dessaint, S.M. Ieee, A. Dekkiche, (2007) 284–289.
[16] J. Unger, C. Hametner, S. Jakubek, M. Quasthoff, J. Power Sources 269 (2014) 883–897.
[17] C. Hametner, S. Jakubek, J. Power Sources 238 (2013) 413–421.
[18] G.L. Plett, J. Power Sources 134 (2004) 252–261.
[19] G.L. Plett, J. Power Sources 134 (2004) 262–276.
[20] G.L. Plett, J. Power Sources 134 (2004) 277–292.
[21] M.A. Roscher, D.U. Sauer, J. Power Sources 196 (2011) 331–336.
[22] T. Huria, G. Ludovici, G. Lutzemberger, J. Power Sources 249 (2014) 92–102.
[23] H. He, R. Xiong, J. Fan, Energies 4 (2011) 582–598.
[24] H. Rahimi-Eichi, F. Baronti, M.-Y. Chow, in: Ind. Electron. (ISIE), 2012 IEEE Int. Symp, 2012, pp. 1336–1341.
[25] Y.-H. Chiang, W.-Y. Sean, J.-C. Ke, J. Power Sources 196 (2011) 3921–3932.
[26] A.H. Ranjbar, A. Banaei, A. Khoobroo, B. Fahimi, Smart Grid IEEE Trans. 3 (2012) 360–367.
[27] J. Kim, B. Cho, Veh. Technol. IEEE Trans. 60 (2011) 4249–4260.
[28] C.R. Gould, C.M. Bingham, D.A. Stone, P. Bentley, IEEE Trans. Veh. Technol. 58 (2009) 3905–3916.
[29] T. Kim, W. Qiao, Energy Convers. IEEE Trans. 26 (2011) 1172–1180.
[30] M. Sitterly, L.Y. Wang, G.G. Yin, C. Wang, Sustain. Energy IEEE Trans. 2 (2011) 300–308.
[31] D. Andre, M. Meiler, K. Steiner, H. Walz, T. Soczka-Guth, D.U. Sauer, J. Power Sources 196 (2011) 5349–5356.
[32] PNGV Battery Test Manual, U.S. Department of Energy, 2001.
[33] S. Wang, M. Verbrugge, J.S. Wang, P. Liu, J. Power Sources 196 (2011) 8735–8741.
[34] G. Plett, Veh. Technol. IEEE Trans. 53 (2004) 1586–1593.
[35] L.W. Juang, P.J. Kollmeyer, T.M. Jahns, R.D. Lorenz, in: Energy Convers. Congr. Expo. (ECCE), 2012 IEEE, 2012, pp. 1819–1826.
[36] L.E. Unnewehr, S.A. Nasar, in:, John Wiley & Sons, Inc., New York, 1982, pp. 81–91.
[37] D. Linden, T.B. Reddy, Linden's Handbook of Batteries, Fourth, McGraw-Hill Education, New York, 2010.
[38] V.H. Johnson, J. Power Sources 110 (2002) 321–329.
[39] M.S.R. Khatib, A.L. Dalverny, M.L.D.M. Gaberscek, J. Phys. Chem. 117 (2013) 837–849.
[40] A.A.-H. Hussein, N. Kutkut, I. Batarseh, in: 2011 Twenty-Sixth Annu. IEEE Appl. Power Electron. Conf. Expo, 2011, pp. 1790–1794.
[41] S. Schwunk, N. Armbruster, S. Straub, J. Kehl, M. Vetter, J. Power Sources 239 (2013) 705–710.
[42] A.J. Fairweather, M.P. Foster, D.A. Stone, J. Power Sources 207 (2012) 56–59.
[43] M. Shahriari, M. Farrokhi, IEEE Trans, Ind. Electron 60 (2013) 191–202.
[44] B.S. Bhangu, P. Bentley, D.A. Stone, C.M. Bingham, in: Veh. Power Propulsion, 2005 IEEE Conf, 2005, p. 10.
[45] C. Gould, J. Wang, D. Stone, M. Foster, in: Int. Symp. Power Electron. Power Electron. Electr. Drives, Autom. Motion, 2012, pp. 353–358.
[46] H. Rahimi-eichi, S. Member, M. Chow, (2012).
[47] F. Sun, R. Xiong, H. He, J. Power Sources 259 (2014) 166–176.
[48] M.A. Roscher, O.S. Bohlen, D.U. Sauer, Energy Convers. IEEE Trans. 26 (2011) 737–743.
[49] S. Nejad, D.T. Gladwin, D.A. Stone, in: Ind. Electron. Soc. IECON 2014-40th Annu. Conf. IEEE, 2014, pp. 5660–5665.
[50] J. Remmlinger, M. Buchholz, M. Meiler, P. Bernreuter, K. Dietmayer, J. Power Sources 196 (2011) 5357–5363.
[51] M. Ouyang, G. Liu, L. Lu, J. Li, X. Han, J. Power Sources 270 (2014) 221–237.
[52] C.Y. Chun, J. Baek, G.-S. Seo, B.H. Cho, J. Kim, I.K. Chang, S. Lee, J. Power Sources 273 (2015) 255–263.
[53] R.E. Kalman, Trans. ASME J. Basic Eng. 82 (1960) 35–45.
[54] I. Kim, IEEE Trans. Power Electron 25 (2010) 1013–1022.
[55] J. Kim, S. Lee, B.H. Cho, Power Electron. IEEE Trans. 27 (2012) 436–451.
[56] D. Andre, C. Appel, T. Soczka-Guth, D.U. Sauer, J. Power Sources 224 (2013) 20–27.
[57] R. Xiong, X. Gong, C.C. Mi, F. Sun, J. Power Sources 243 (2013) 805–816.
[58] Y. He, X. Liu, C. Zhang, Z. Chen, Appl. Energy 101 (2013) 808–814.
[59] L. Zhong, C. Zhang, Y. He, Z. Chen, Appl. Energy 113 (2014) 558–564.
[60] J. Remmlinger, M. Buchholz, T. Soczka-Guth, K. Dietmayer, J. Power Sources 239 (2012) 689-395.
[61] J. Du, Z. Liu, Y. Wang, Control Eng. Pract. 26 (2014) 11–19.
[62] F. Auger, M. Hilairet, J.M. Guerrero, E. Monmasson, T. Orlowska-Kowalska, S. Katsura, Ind. Electron. IEEE Trans. 60 (2013) 5458–5471.
[63] H. He, R. Xiong, X. Zhang, F. Sun, J. Fan, Veh. Technol. IEEE Trans. 60 (2011) 1461–1469.
[64] C. Hu, B.D. Youn, J. Chung, Appl. Energy 92 (2012) 694–704.
[65] D. Andre, a. Nuhic, T. Soczka-Guth, D.U. Sauer, Eng. Appl. Artif. Intell. 26 (2013) 951–961.
[66] B. Pattipati, C. Sankavaram, K.R. Pattipati, Syst. Man. Cybern. Part C Appl. Rev. IEEE Trans. 41 (2011) 869–884.
[67] M. Green, J.B. Moore, Am. Control Conf. 1985 (1985) 412–417.
[68] Y. Zhu, in: Multivariable Syst. Identif. Process Control, First, Elsevier Science Ltd, Oxford, 2001, pp. 41–52.
[69] V.V. Chalam, Adaptive Control Systems: Techniques and Applications, Marcel Dekker, Inc., New York, 1987.